Eastern Equatorial Pacific SST Variability: ENSO and Non-ENSO Components and Their Climatic Associations

ALBERTO M. MESTAS-NUÑEZ

Cooperative Institute for Marine and Atmospheric Studies, University of Miami, Miami, Florida

DAVID B. ENFIELD

NOAA/Atlantic Oceanographic and Meteorological Laboratory, Miami, Florida

(Manuscript received 1 September 1999, in final form 10 March 2000)

ABSTRACT

Using an updated Kaplan et al. global SST anomaly (SSTA) dataset (1870–1999) a canonical representation of El Niño–Southern Oscillation (ENSO) is constructed. When this canonical ENSO is subtracted from the data, a residual (non-ENSO) dataset for SSTA is left that includes interseasonal to multidecadal variability. Over the eastern equatorial Pacific (Niño-3) the canonical ENSO accounts for about 79% of the total SSTA variability, and the residual, dominated by decadal timescales, accounts for the rest. In particular, about 40%–50% of the amplitudes of the strong 1982–83 and 1997–98 El Niño events were accounted for by the residual variability. The non-ENSO variability is characterized by the known shift from cold to warm eastern tropical Pacific in the mid- to late 1970s as well as by a (nonstationary) interannual variance increase during the 1980s and 1990s.

Composite maps of surface (SST, sea level pressure, and winds) and tropospheric (divergent winds, velocity potential, and vertical velocity) variables are used to compare the spatial patterns characterizing the canonical ENSO and the residual components of the Niño-3 variability. The residual composites are found to only share large-amplitude fluctuations of SST anomalies in the equatorial Pacific east of the date line. When these composites are separated into decadal and interannual components, the decadal part closely resembles the structure of the Pacific decadal oscillation. The major patterns of tropospheric variability associated with the ENSO and decadal non-ENSO components are very different. At low latitudes, they imply nearly opposite impacts on far-field regional climates, based on their respective warming (or cooling) phases within the Niño-3 region. This unexpected result for low-latitude climate associations runs contrary to the naive expectation (recently shown to be true for North America) that a decadally warm tropical east Pacific will reinforce the climate effects associated with ENSO alone. This indicates that, in the Tropics, climate outlooks may be more accurate if based on separately analyzed relationships between these SSTA components and their associated climate fluctuations.

1. Introduction

Although the largest signal in global SST anomaly (SSTA) variability is the interannual El Niño–Southern Oscillation (ENSO), other signals in the SSTA record (viz., global warming and decadal-to-multidecadal variability) can also have important climatic effects. For example, the fact that two of the largest ENSO events (1982–83 and 1997–98) have occurred in the space of 15 years, at the end of the twentieth century, suggests that ENSO activity is on the rise, perhaps due to global warming. Even before the 1997–98 episode, Trenberth and Hoar (1996, 1997) argued this to be the case, noting that recurring but smaller warmings in the years following the 1991–92 El Niño are unprecedented in the historical record. However, other scientists believe that the recent increase in ENSO activity may not be unique in the historical (instrumental and proxy) record, suggesting that it may be related to natural variability (Harrison and Larkin 1997; Rajagopalan et al. 1997; Allan and D'Arrigo 1999).

Latif et al. (1997) attributed the unusual ENSO activity of the 1990s to the warm phase of a Pacific decadal mode of variability. Consistent with this, when the 1856–1991 SSTA data are bandpassed (1.5–8 yr) and an ENSO mode is extracted for the globe (separated from decadal variability and trends), there are no apparent differences in ENSO behavior between the most recent decades and the decades around the turn of the nineteenth century (Enfield and Mestas-Nuñez 1999).

Because SSTA variability that is unrelated to ENSO can have significant climatic effects that may be masked by the dominant ENSO signal, our approach to studying the global SSTA variability has been to separate the canonical ENSO from the residual variability (referred

Corresponding author address: A. M. Mestas-Nuñez, NOAA/AOML, 4301 Rickenbacker Causeway, Miami, FL 33149.
E-mail: mestas@aoml.noaa.gov

to as non-ENSO), which includes noncanonical ENSO as well as decadal and longer-period variability. The canonical ENSO signal was extracted from an SSTA dataset that is more than a century long using a complex version of EOF analysis that allows for phase propagation. The canonical ENSO variability was defined as the leading complex EOF of SSTA in the 1.5–8-yr band (Enfield and Mestas-Nuñez 1999, 2000); note that we group together the quasi-biennial (2–2.5 yr) and lower-frequency (2.5–7 yr) ENSO signals (e.g., Allan 2000). This global ENSO mode, which captures well-known aspects of ENSO, was removed from a 1.5-yr low-pass version of the data to generate the non-ENSO residuals. The detrended non-ENSO variability was studied using unrotated and rotated EOFs and was shown to be dominated by global-scale, decadal-to-multidecadal signals with significant atmospheric associations (Enfield and Mestas-Nuñez 1999, 2000; Mestas-Nuñez and Enfield 1999).

The main goal of this paper is to investigate and compare the atmospheric signatures associated with the ENSO and non-ENSO (residual) components of the SSTA variability in the eastern equatorial Pacific. Compared to our previous analyses of SSTA we now include higher frequencies in both ENSO and non-ENSO variability (scales shorter than 1.5 yr) and use an updated dataset that includes the recent 1997–98 El Niño event. The data and methods are presented in section 2. The ENSO and non-ENSO components of the variability in the eastern equatorial Pacific are described in section 3. The associated surface and tropospheric patterns are presented in sections 4 and 5, respectively. The paper ends with concluding remarks and discussion in section 6.

2. Data and methods

The main dataset used in this study is the reconstruction of historical SSTA generated by Kaplan et al. (1998, hereinafter K98) on a $5^\circ \times 5^\circ$ grid. The K98 reconstruction uses optimal estimation in the space of 80 EOFs to interpolate ship observations from the U.K. Met. Office database (Parker et al. 1994). These observations are monthly deviations from the 1951–80 climatology for the period 1856–1991. An extended version of the K98 dataset is now available online at the International Research Institute for Climate Prediction/Lamont-Doherty Earth Observatory Climate Data Library. For 1856–1981 this is the same as in K98 but after (November) 1981 the extended dataset is the projection of the $1^\circ \times 1^\circ$ optimally interpolated product of Reynolds and Smith (1994) (which combines ship observations with remote sensing data) on the same set of 80 EOFs used by K98.

Because the quality of SSTA reconstructions prior to about 1870 is questionable (Smith et al. 1998), we use the more reliable period that starts in 1870 for the analysis performed here. The resulting SSTA dataset used in this analysis is gridded on the same $5^\circ \times 5^\circ$ K98 grid and covers the period January 1870–December 1999. Frequently in this paper we refer to our previous analyses of the K98 data that have been published elsewhere. Analyses of the entire 1856–1991 K98 period were presented in Enfield and Mestas-Nuñez (1999) and Mestas-Nuñez and Enfield (1999), of the shorter 1870–1991 period in Enfield and Mestas-Nuñez (2000), and of the longer 1856–1996 period, with appended Reynolds and Smith data, in Landsea et al. (1999).

To separate the interannual and decadal bands (scales shorter and longer than 8 yr) of SSTA variability in section 3, we use a one-dimensional locally weighted regression (loess) algorithm (Cleveland and Devlin 1988). With this filter, each smoothed estimate is obtained by a weighted least squares fit of a quadratic curve to the raw data near the estimation time. Therefore we do obtain estimates at the end points of the time series but they are less reliable because less data go into the least squares fitting. To ameliorate the effects of the filtering near the end of the record we performed the filtering and ENSO/non-ENSO separation using the complete January 1870–December 1999 extended K98 dataset but choose to present and base our statistics on the shorter January 1870–January 1999 period.

Throughout the paper we extract associations by constructing differences of composite means of surface and tropospheric (upper air) boreal winter variables based on the phases of the updated K98 SSTA averaged over the Niño-3 region (5°S–5°N, 150°–90°W). The threshold for defining the warm and cold phases of the Niño-3 SSTA indexes is $\pm 0.1^\circ$C, but the results are not very sensitive to moderate changes in the value of this threshold. The composites are constructed using two components of the Niño-3 SSTA variability. One component is the Niño-3 average SSTA reconstructed from a complex EOF mode that reproduces the global characteristics of ENSO-related SSTA variability (Enfield and Mestas-Nuñez 1999). The second component is simply the residual Niño-3 SSTA after the global ENSO reconstruction is subtracted. The ENSO component is highly interannual, but the residual contains both decadal and interannual timescales. Because we wish to compare and contrast the canonical ENSO variability with the non-ENSO variability, and because ENSO and its tropospheric teleconnections are consistently stronger during the boreal winter, we have chosen to do our analysis for the December–January–February (DJF) season. Furthermore, because the two timescales might be quite different in their spatiotemporal associations, the analyses of the residual variability were done separately for both the low-pass (decadal, scales longer than 8 yr) and high-pass (interannual, scales shorter than 8 yr) portions. The distinctions turned out to be significant in the surface analysis but not in the tropospheric analysis.

We choose composite analysis instead of the associated correlation pattern approach because it preserves physical units and has the virtue of simplicity. It also

avoids the pitfalls of false associations that can occur in global multivariate analyses such as that of Enfield and Mestas-Nuñez (1999) and as explained by Mestas-Nuñez and Enfield (1999). In this analysis the significance of associations identified through composite averages can be judged because we are already familiar with many aspects of the climate response to ENSO, while the strength of the response to the residual (non-ENSO) variability can be judged by comparison to ENSO. Nevertheless, we also compute statistical confidence intervals for the composite difference fields throughout the paper.

For the surface analyses, we used SST, sea level pressure (SLP) and surface vector wind stress from the version of the Comprehensive Ocean–Atmosphere Data Set (COADS) produced at the University of Wisconsin—Milwaukee (UWM) by da Silva et. al (1994, hereinafter referred to as UWM/COADS). UWM/COADS includes corrections to reduce wind speed bias and artificial trends known to exist in the COADS data (e.g., Cardone et al. 1990) and consists of monthly $1^\circ \times 1^\circ$ objectively analyzed fields for the period 1945–93. We calculated long-term average seasonal cycles using the same 1951–80 averaging period as in the K98 climatology and removed them to generate monthly anomalies of SST, SLP, and vector wind stress. The monthly anomalies were temporally averaged to generate 3-month (DJF) boreal winter anomalies.

For the tropospheric analyses, we obtained the following 3-month averaged (DJF) atmospheric variables for 50 boreal winters from 1949–50 to 1998–99, from the National Centers for Environmental Prediction–National Center for Atmospheric Research (NCEP–NCAR) reanalysis (Kalnay et al. 1996): velocity potential at 850 and 200 hPa, and pressure vertical velocity at 500 hPa. The three levels were chosen as representative of the lower, upper, and midtroposphere, respectively, and because more data are available for the reanalysis assimilation at 850 hPa (cloud motions in the Tropics) and 200 hPa (high-altitude aircraft). The divergent (irrotational) component of the wind field at 850 and 200 hPa was derived by computing the gradient of the velocity potential at the respective pressure levels. Consistent with the surface variables, we calculated long-term temporal averages of the 3-month averaged data using the same 1951–80 averaging period as the K98 climatology and removed them to generate winter anomalies of all the tropospheric variables.

3. SSTA variability in the eastern tropical Pacific

The global ENSO mode can be interpreted as a canonical representation of the spatial and temporal commonalities found in the ENSO band of the historical SSTA data. In our early work, the ENSO mode was defined as the first complex EOF of the 1856–1991 K98 SSTA in the 1.5–8-yr band (Enfield and Mestas-Nuñez 1999). Later, we recomputed the ENSO mode using the same definition but for the more reliable 1870–1991 period of the K98 data and obtained very similar results (Enfield and Mestas-Nuñez 2000).

In this paper, we introduce two minor modifications to our previous ENSO-mode calculations. First, we redefine the ENSO mode as the leading complex EOF in the 0–8-yr (instead of 1.5–8 yr) band. This definition includes within the ENSO band high-frequency (0–1.5 yr) intraseasonal variability, which accounts for multiple peaks and other shorter-period structures often seen in extreme ENSO events. Second we now use an extended version of the K98 dataset (obtained as described in section 2) for the 1870–1999 period. The extension of the K98 dataset based on Reynolds and Smith data allows inclusion in the analysis of the recent strong 1997–98 El Niño event.

With the above modifications, the recalculated ENSO mode accounts for 20.4% of the global SSTA variance in the 0–8-yr band. The patterns of spatial amplitude and phase (Figs. 1a,b) are almost identical to our previous representations (Enfield and Mestas-Nuñez 1999). This indicates that the ENSO mode is robust and does not depend on the high-frequency content, nor on minor changes in the record length. The time realization of the ENSO mode, constructed as the average of the mode-reconstructed SSTA in the Niño-3 region (indicated with the rectangle in Fig. 1b) is shown in Fig. 1c. As expected, the time series of the ENSO-mode shows more realistic shorter-period fluctuations when compared with our earlier smooth depictions of the Niño-3 variability. Part of this high-frequency content may be related to transient 30–60 day oscillations that are very common in the Tropics but that are not the focus of this research (e.g., Madden and Julian 1994).

The Niño-3 SSTA variability is decomposed into canonical ENSO and non-ENSO residual variability in Fig. 2; we did not detrend the residuals because the contribution of the trend to the eastern equatorial Pacific variability is small (see Fig. 1 of Enfield and Mestas-Nuñez 1999). The raw average of SSTA in the Niño-3 region, which is sometimes used as an index of ENSO, is shown in Fig. 2a. This index is inversely correlated to the more traditional Southern Oscillation index (SOI), the atmospheric SLP difference between the southeastern tropical Pacific and the Indo–Australian region. The ENSO mode time series is shown in Fig. 2b (same as Fig. 1c), and the residual time series is shown in Fig. 2c (i.e., the difference of the time series in Fig. 2a minus the time series in Fig. 2b). The temporal correlation coefficient between the ENSO and non-ENSO time series in Figs. 2b and 2c is 0.05, indicating that these time series are approximately linearly independent. Furthermore, the temporal correlations of these time series with the straight Niño-3 SSTA index in Fig. 2a are 0.89 and 0.50, respectively. This indicates that the ENSO mode accounts for approximately 78.6% of the total Niño-3 SSTA variance and the residual variability accounts for the rest.

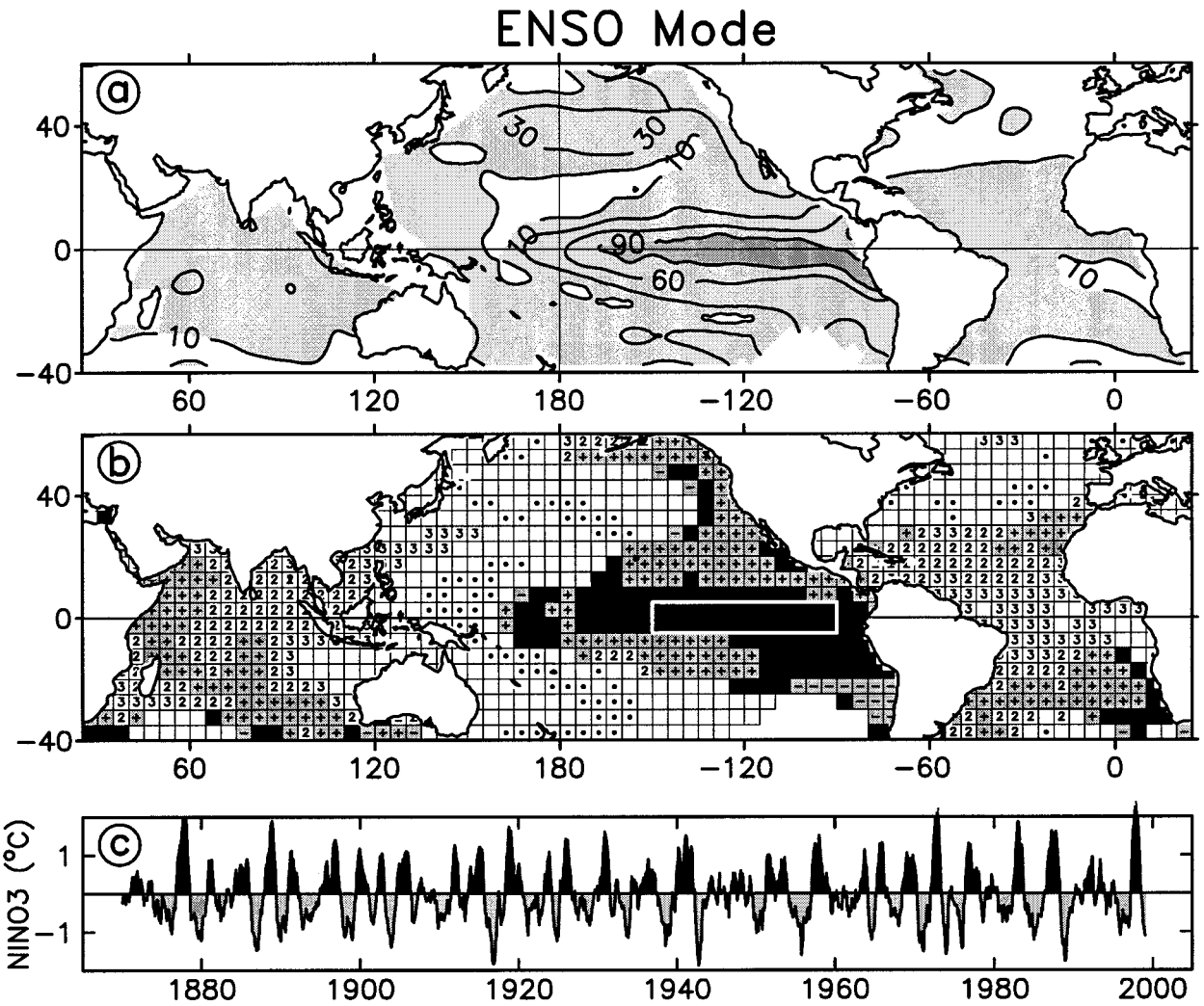

FIG. 1. First complex EOF, describing the global ENSO variability. (a) Spatial distribution of the amplitude with respect to the modal reconstruction over the Niño-3 index region (white rectangle, middle panel). Contours shown are 10, 30, 60, and 90. A score of 100 is the average amplitude over the Niño-3 region. (b) Spatial distribution of phase lag (seasons) constructed using a nominal periodicity of 44 months (Enfield and Mestas-Nuñez 1999); + (−) indicates that the data lags (leads) Niño-3 (lower panel) by one season, and positive numbers indicate data lags of more than one season. Black dots indicate squares with phases approximately opposite to the Niño-3 region (180° ± 12.5°). (c) Temporal reconstruction of the mode-related variability averaged over the Niño-3 region.

An interesting feature of Fig. 2 is that the non-ENSO residual SSTA time series in Fig. 2c has warm peaks that coincide with the 1982–83 and 1997–98 El Niño events in Fig. 2b. To estimate the relative contribution of the residuals to the total SSTA amplitude, we compared the 1982–83 and 1997–98 DJF averages of the total and residual monthly time series in Figs. 2a and 2c. The respective amplitude ratios are 0.45 and 0.38, indicating that about 40%–50% of the amplitudes of the record-setting 1982–83 and 1997–98 El Niño events were accounted for by the residual variability.

In Fig. 3, the residual Niño-3 SSTA variability was further decomposed into high-pass and low-pass components, describing residual variability with periods shorter and longer than 8 yr, respectively. The original residual Niño-3 time series from Fig. 2c is shown again in Fig. 3a but with a stretched *y* axis. The high-pass time series in Fig. 3b was obtained by removing the ENSO mode from a high-pass version of the updated K98 dataset (i.e., with scales longer than 8 yr removed) and averaging these data in the Niño-3 region. The low-pass time series was obtained by removing the high-pass time series in Fig. 3b from the original residual time series in Fig. 3a. The respective correlations between the time series in Figs. 3b and 3c, and the straight Niño-3 SSTA time series in Fig. 2a, are 0.29 and 0.41, indicating that they explain about 8.6% and 16.8% of its variance. These figures indicate that the fraction of the raw Niño-3 SSTA variance explained by the low-pass residual component is about twice the fraction ex-

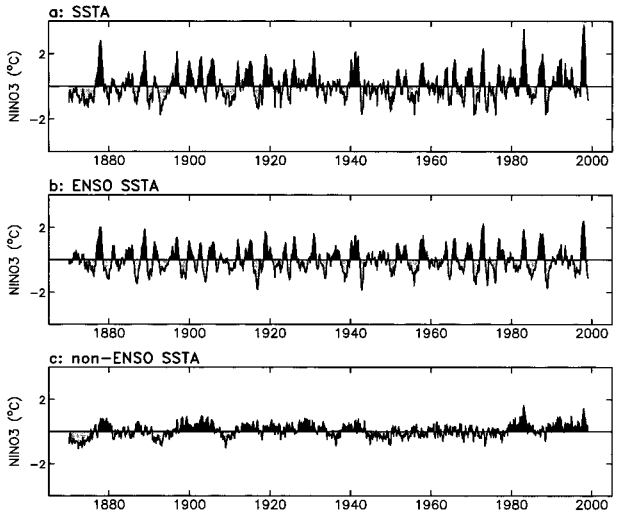

FIG. 2. Decomposition of (a) the area-averaged SSTA into (b) its ENSO (same as Fig. 1c) and (c) non-ENSO (residual) components, in the Niño-3 region.

plained by the high-pass residual component. In summary, the original Niño-3 SSTA variance is divided approximately into ENSO mode 78.6%, low-pass residual 16.8%, and high-pass residual 8.6%.

Qualitatively, the Niño-3 high-pass time series in Fig. 3b appears to have larger amplitudes after 1980. To check if this apparent amplitude increase in the high-pass residuals is significant we computed the ratio of the variance in each successive 20-yr period starting in 1880 to the variance in the full record (high-pass column in Table 1). For comparison, we also calculated the respective variance ratios for the ENSO mode time series (ENSO column in Table 1); similar ratios for the non-ENSO total and low-pass time series were not computed

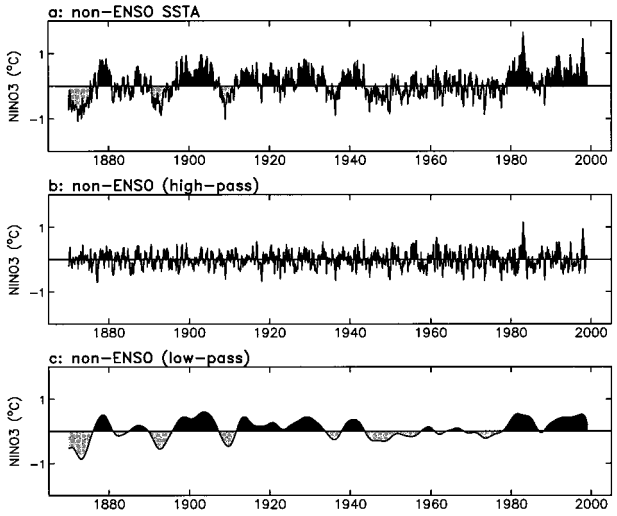

FIG. 3. Decomposition of (a) the area-averaged SSTA residuals (same as Fig. 2c, but with stretched *y* axis) into its (b) high-pass and (c) low-pass components in the Niño-3 region.

TABLE 1. Ratio of Niño-3 SSTA variances for successive 20-yr periods to the variance calculated for the full record length for the ENSO mode and the non-ENSO high-pass residuals. Significant ratios at the 99% level from an *F* test are indicated with *.

Year	ENSO	High-pass residuals
1880–99	1.01	0.93
1900–19	0.99	0.69 (*)
1920–39	0.71 (*)	0.84
1940–59	0.87	1.03
1960–79	1.06	1.09
1980–99	1.33 (*)	1.55 (*)

because they are highly decadal and the record is too short to investigate changes in decadal statistics with time. The ENSO variance shows a significant decrease in 1920–39 and a significant increase in 1980–99, consistent with the wavelet-analysis results of Torrence and Compo (1998). The high-pass variance shows a decrease in 1900–19 and a very large increase in 1980–99. The very large variance increase in the high-pass residuals after 1980 suggests that this time series may be nonstationary, but this may also be associated with increased sampling during the satellite era.

In comparison with the unrotated (U) and rotated (R) EOFs of Enfield and Mestas-Nuñez (1999) and Mestas-Nuñez and Enfield (1999), the Niño-3 residual (non-ENSO) variability correlates better with the eastern tropical Pacific rotated mode R3 and the central tropical Pacific interdecadal rotated mode R4 (Table 2, column 1). When the residuals are separated into low-pass and high-pass components, the high-pass residuals correlate poorly with all the rotated and unrotated modes (Table 2, column 2). On the other hand, the correlations of the low-pass residuals with R3 and R4 increase, as shown in the third column of Table 2. According to Mestas-Nuñez and Enfield (1999), R3 was associated with an interdecadal modulation of ENSO, while R4 was associated with interdecadal aspects of the Pacific decadal oscillation (PDO). Both of these phenomena are thus present in the residual non-ENSO variability. Note that the low-pass correlations with the rotated modes (R3 and R4) are essentially linear combinations of contributions seen in the unrotated modes (U1, U2, and U3)

TABLE 2. Temporal correlation of the non-ENSO (residual) time series and its high- and low-pass components with the leading unrotated (U) and rotated (R) EOFs of Enfield and Mestas-Nuñez (1999) and Mestas-Nuñez and Enfield (1999).

Mode	Residuals	High-pass	Low-pass
U1	0.37	−0.08	0.54
U2	−0.41	−0.06	−0.58
U3	−0.33	−0.10	−0.34
R1	−0.03	−0.02	−0.02
R2	0.18	−0.11	0.32
R3	0.56	0.09	0.65
R4	0.55	−0.05	0.74
R5	−0.21	0.16	−0.40
R6	−0.14	−0.03	−0.15

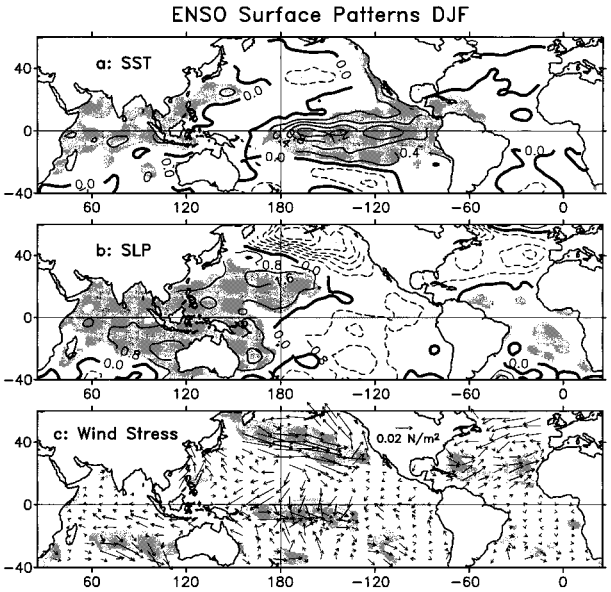

FIG. 4. Boreal winter (DJF) differences between composite averages with respect to the positive and negative values of the ENSO time series in Figs. 1c and 2b for (a) SST, (b) SLP, and (c) surface wind stress. Contour intervals for SST and SLP are 0.4°C and 0.8 hPa, respectively. Significant positive (negative) differences in SST, SLP, and zonal wind stress are heavily (lightly) shaded.

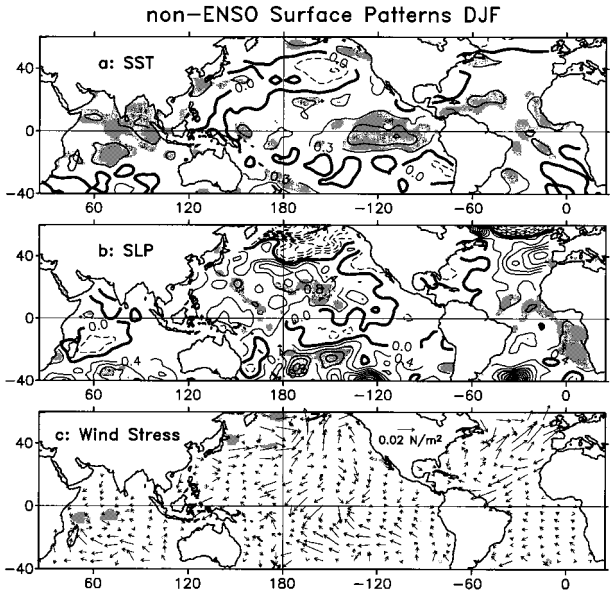

FIG. 5. As in Fig. 4, but for the DJF averages of the time series in Fig. 3a and with contour intervals for SST and SLP equal to 0.3°C and 0.4 hPa, respectively.

but optimized to the eastern and central equatorial Pacific regions by the varimax rotation procedure. The reader is referred to Mestas-Nuñez and Enfield (1999) for a more complete discussion of the unrotated and rotated modes and their relationships to climate oscillations discussed elsewhere in the literature.

4. Associated surface patterns

In this section, we show contour plots of SST and atmospheric surface patterns (SLP and wind stress) associated with the global ENSO (Fig. 4) and residual (non-ENSO) components of SSTA (Fig. 5) introduced in section 3. These patterns are constructed as the boreal winter (DJF) composites (warm minus cold) of the UWM/COADS data on the respective Niño-3 time series in Figs. 2 and 3. Positive (negative) contours are indicated with solid (dashed) lines and 95%-significant positive (negative) differences from a *t* test are indicated with dark (light) gray shading at every grid point.

a. The canonical ENSO patterns

The SST, SLP, and wind stress patterns associated with the Niño-3 time series of the global ENSO mode are shown in Fig. 4. The ENSO patterns shown in this section are very similar to the regression patterns obtained by Zhang et al. (1997) and Garreaud and Battisti (1999) using a 6-yr high-pass filtered cold tongue index; their cold tongue index is the average SSTA in the region between 6°S–6°N and 180°–90°W and is highly correlated to the Niño-3 index shown in Fig. 2a.

Figure 4a shows the SSTA spatial structure at the peak (DJF) of the El Niño (warm) phase of ENSO. This pattern is similar to Figs. 1a and 1b except that it only shows regions of in-phase (positive) or out-of-phase (negative) relationships relative to Niño-3 variability; this is the common picture obtained using standard rather than complex EOF analysis. The larger SSTA amplitudes are found in the central tropical Pacific, with smaller out-of-phase anomalies at the extratropical midlatitudes. Small positive SSTAs are also found in the Indian and tropical North Atlantic Oceans.

In the central equatorial Pacific, the SLP and wind anomaly differences (Figs. 4b,c) show the surface expression of the zonal Walker cell, with eastward pressure gradient anomalies driving westerly wind anomalies. In the midlatitude North Pacific, the SLP and wind anomaly differences show strong anticyclonic circulation over the western side of the basin, consistent with an intensification of subsidence in the descending branch of the meridional Hadley circulation. Some evidence of a similar but smaller pattern is also seen in the western midlatitude South Pacific. These off-equatorial patterns in the western Pacific may play an important role in the evolution of ENSO (Wang et al. 1999). In the subpolar North Pacific, there are strong cyclonic anomalies that suggest an intensification of the Aleutian low.

In the Atlantic, the SSTA differences are significant only in the western tropical North Atlantic and the intra-Americas Sea, capturing the initial propagation of the ENSO signal into the Atlantic basin. These SSTA dif-

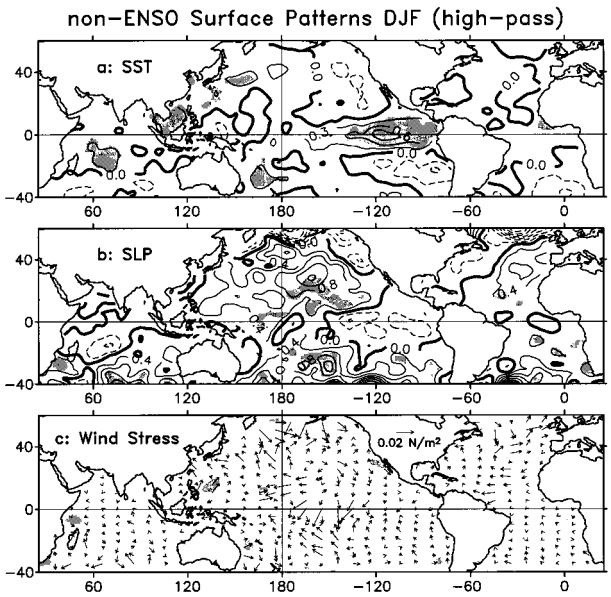

FIG. 6. As in Fig. 4, but for the DJF averages of the time series in Fig. 3b and with contour intervals for SST and SLP equal to 0.3°C and 0.4 hPa, respectively.

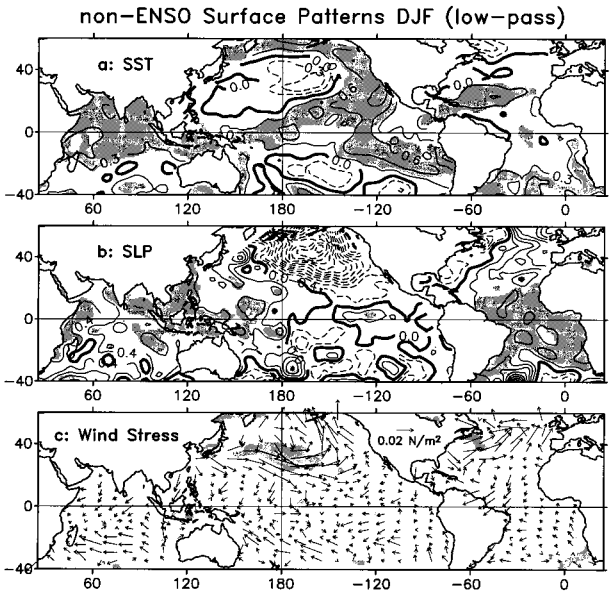

FIG. 7. As in Fig. 4, but for the DJF averages of the time series in Fig. 3c and with contour intervals for SST and SLP equal to 0.3°C and 0.4 hPa, respectively.

ferences are associated with cyclonic wind and SLP anomalies over the midlatitude North Atlantic.

b. The non-ENSO residual patterns

The surface patterns associated with the residual (non-ENSO) time series shown in Fig. 3a are shown in Fig. 5. In general the composite differences are only significant at low latitudes, except for SLP anomaly differences at mid/high southern latitudes, where the quality of the data is questionable. In the Tropics, the SSTA difference pattern is similar to the ENSO pattern but the pressure and winds are quite different. This seems to contradict the results of Zhang et al. (1997) and Garreaud and Battisti (1999), who found similar SST, SLP, and surface wind stress patterns associated with the (ENSO related) interannual and interdecadal components of the leading EOF of global SSTA. However, their leading global EOF modes may have filtered out smaller-scale spatial SSTA variability that may have a significant contribution. The partition of our residuals into high-pass and low-pass components is helpful in explaining the apparent discrepancies with the Zhang et al. (1997) and Garreaud and Battisti (1999) results.

We note that the post–World War II portion of the residual time series (Figs. 2c and 3a) undergoes a sharp shift, from near-zero or negative values to large positive values, in the late 1970s. This shift was used by Lau and Weng (1999) to construct a difference composite of SSTA based on 1977–96 minus 1955–76. While the spatial pattern of Fig. 5 does resemble the Pacific decadal pattern described by others (e.g., Latif and Barnett 1994; Zhang et al. 1997), it is more clearly like the difference map of Lau and Weng (1999), with larger anomalies in the eastern low-latitude Pacific. It is also more characteristic of the rotated mode (R3) of Mestas-Nuñez and Enfield (1999) and is consistent with the high correlation between the Niño-3 residual and R3 (Table 2). As we show below, however, low-pass filtering shifts the resemblance more in the direction of the classic Pacific decadal variability.

The patterns associated with the high-pass residuals are shown in Fig. 6. The SSTA pattern (Fig. 6a) shows significant positive anomalies in small regions in the eastern tropical Pacific, in the western boundary current regions of the subtropical North and South Pacific (i.e., in the Kuroshio extension and the East Australia Current regions), and in the southern Indian Ocean (10°–20°S). Significant negative differences are found near the coast of South America and near the Gulf of Alaska. The SLP and wind stress patterns (Figs. 6b,c) do not show significant differences, except in the midlatitude subtropical North and South Pacific where there is some evidence of anticyclonic forcing. Although anticyclonic forcing at midlatitudes is consistent with warm anomalies advected by the western boundary currents of the subtropical gyres, the localized nature of the western Pacific midlatitude features suggests that they may just be the result of geophysical noise.

The patterns associated with the low-pass residuals (Fig. 7) show both similarities and differences with the global ENSO patterns, and can be easily identified with the Pacific decadal variability that has been described by others. The SSTA pattern is generally similar to that of ENSO, with warming in the eastern tropical Pacific and an anticorrelated region of cooling in the west-cen-

tral North Pacific. However, the warming covers a broader latitudinal scale and is not concentrated near the equator, as with ENSO, while the cooling in the central North Pacific is notably more intense and well defined. The pattern is very similar to that of Latif and Barnett (1994), Zhang et al. (1997), and Mantua et al. (1997), which has been variously referred to as the PDO. Quite different scenarios, such as Latif and Barnett (1996), Gu and Philander (1997), and Kleeman et al. (1999), have been proposed to explain the decadal variability, and it is fair to say that the actual mechanisms involved have not been conclusively identified. A comprehensive summary and discussion of current research on Pacific decadal variability is given by Allan (2000).

We note that the effect of the low-pass filter is to modify the SSTA pattern from the unfiltered one (Fig. 5), which correlates with the eastern equatorial Pacific rotated mode (R3) of Mestas-Nuñez and Enfield (1999), to that of Fig. 7, which resembles more the unrotated decadal mode (U1) of Enfield and Mestas-Nuñez (1999). The latter mode was specifically characterized in terms of the previously identified PDO. While the spatiotemporal variability of these modes shows important differences, they are temporally correlated (not orthogonal in time) and both are dominated by low-latitude cooling (warming) before (after) the mid- to late 1970s. This decadal shift is the essence of the Niño-3 residual variability, and as a low-frequency characteristic it can be most closely identified with the PDO.

Other similarities and differences can be seen between Figs. 4 (global ENSO) and 7 (low-pass residual). The wind distributions, as with SSTA, are broadly similar, for example. This similarity between ENSO and the PDO is also consistent with Zhang et al. (1997) and Garreaud and Battisti (1999). Garreaud and Battisti also point out that although the PDO and ENSO have similar surface wind anomaly patterns, the anomalies in the surface wind divergence are quite different. The main difference is the lack of organized surface wind–divergence anomaly patterns in the eastern equatorial Pacific for the PDO, consistent with the broader decadal SST anomalies in that region (cf. Figs. 4a and 7a). They argue that these differences may explain the different structure of the Southern Hemisphere tropospheric circulations associated with their ENSO and PDO indices.

5. Associated tropospheric circulations

We have seen that surface anomaly composites (SST, SLP, and wind stress) for the global ENSO and residual components of Niño-3 share some features in common in their geographical distributions, while in other ways they are different. The similarities raise the question of whether the large-scale tropospheric circulation patterns associated with ENSO are also characteristic of the residual variability. If this were the case, it would lend credence to the possibility that the more decadal residual variability involves similar ocean–atmosphere interaction mechanisms to those of ENSO and that the two processes may be somehow linked. Should this not be the case, however, we would suspect that the underlying processes are distinct, and the far-flung climate impacts associated with them around the globe may be very different.

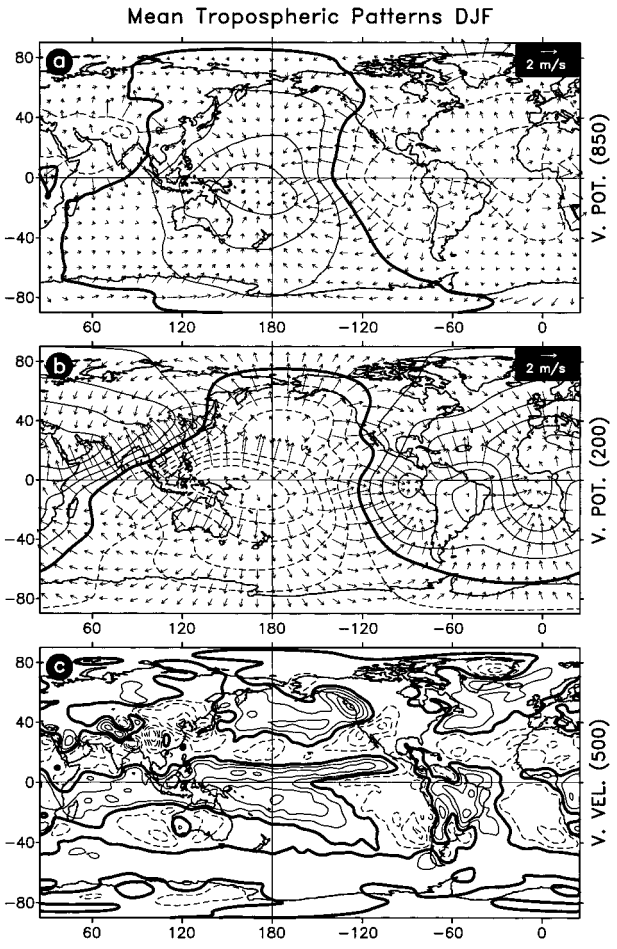

FIG. 8. Long term DJF averages of velocity potential and divergent component of the wind vector at (a) 850 and (b) 200 hPa and (c) the pressure vertical velocity at 500 hPa. The sign of the pressure vertical velocity has been changed so that positive velocities indicate upward motions. The contour intervals for velocity potential and pressure vertical velocity are 2×10^6 m^2 s^{-1} and 2×10^{-2} Pa s^{-1}, respectively.

We also performed the composite analysis using SSTA averaged over the Niño-4 region (5°S–5°N, 160°E–150°W) and found similar but less significant results. We therefore only present the results for Niño-3.

a. The climatic mean

As a template against which to judge the separate ENSO and non-ENSO composites of the anomalous tropospheric direct circulation, we show the mean DJF circulation in Fig. 8. This is the boreal winter velocity potential and divergent component of the wind at 850 (Fig. 8a) and 200 hPa (Fig. 8b), averaged from the

NCEP–NCAR reanalysis (1949–50 through 1998–99). We also show the vertical velocity midway between those two levels, that is, at 500 hPa (Fig. 8c). The distributions show the boreal winter patterns we associate with the classical Walker and Hadley circulations. The Walker circulation is dominated by a low-latitude zonal exchange of air mass between several low-latitude regions of negative (divergent) and positive (convergent) velocity potential. Centers of low-level convergence and high-level divergence just west of the date line and over northern South America are characterized by strong upward velocity at 500 hPa and are well known centers of organized deep convection. Subsidence regions of opposite polarity are seen in the eastern ''cold-ocean'' regions of the Pacific and Atlantic. The meridional Hadley circulations are evident in the northern (winter) hemisphere, with strong northward outflow from the 200-hPa divergent centers toward convergent zonal ridges of velocity potential in the 20°–30°N band over Afro–Asia, the North Pacific, and the North Atlantic. Corresponding bands of midtropospheric subsidence (negative 500-hPa vertical velocity) lie below the zonal ridges of 200-hPa confluence. Similar banded structures are nearly absent in the southern (summer) hemisphere.

b. The canonical ENSO patterns

Figure 9 shows the distribution of the difference between two composite means of the same data seen in Fig. 8: boreal winters (DJF), in which the global ENSO reconstruction for Niño-3 is greater than zero, minus those for which the reconstructed index is less than zero. We now see large differences in the equatorial centers of divergence and convergence, in fact, almost the direct opposite of the normal case in Fig. 8. In particular, regions west of the date line, plus northern South America, are now regions of convergence at 200 hPa and anomalous downward motion at 500 hPa, while the opposite holds true between the dateline and South America. Because of the smaller contour intervals and vector scales used for the anomaly maps, however, these distributions do not represent a nullification or reversal of the average situation in Fig. 8, but rather a significant weakening of it. Specifically, Fig. 9 is consistent with an eastward migration of the normal convective center over Indonesia to a position over the central Pacific near the date line, and with a weakening of the normal Walker circulation at 850 hPa. However, the Walker flow is little changed at 200 hPa between the dateline and the Galapagos Islands.

The northward Hadley flow, and associated convergence over the North Pacific, are considerably increased. Anomalous subsidence affects a large area there, weakening the upward motions that normally characterize the Kuroshio extension region north of 35°N and west of 140°W. It is noteworthy that the normal upward motions over northern South America are also weakened, but only north of the equator in an area that does not include

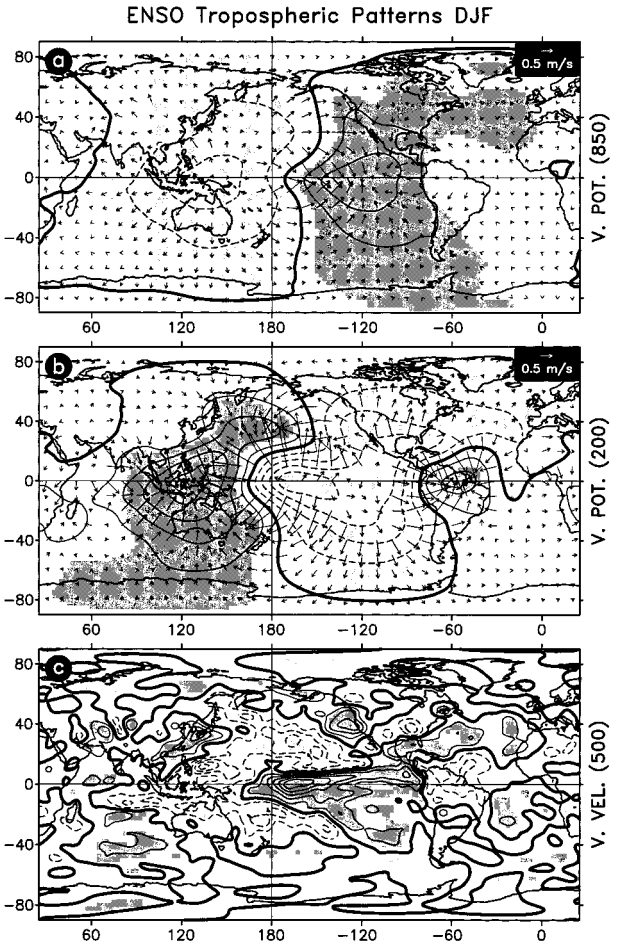

FIG. 9. Differences between composite averages with respect to the time series of the ENSO mode in Figs. 1c and 2b for velocity potential and divergent components of the wind at (a) 850 and (b) 200 hpa and (c) pressure vertical velocity at 500 hPa. The sign of the pressure vertical velocity has been changed so that positive velocities indicate upward motions. The contour intervals for velocity potential and pressure vertical velocity are 8×10^5 m^2 s^{-1} and 8×10^{-3} Pa s^{-1}, respectively.

northeast Brazil. Although we must be cautious about the details of these derived variables in the reanalysis, this suggests that El Niño–related rainfall deficits in northeast Brazil may not be greatly attributable to anomalous subsidence. The alternative mechanism for El Niño–related drought there is the northward displacement of the Atlantic ITCZ in response to El Niño–induced warming in the North Atlantic (Enfield and Mayer 1997). Meanwhile, in Venezuela and Colombia the opposite is probably true, with subsidence effects being very strong. We note that this feature over South America is associated with a weakening of the North Atlantic Hadley cell.

c. The non-ENSO residual patterns

When composite maps are constructed for the low-pass (decadal) component of the residual variability

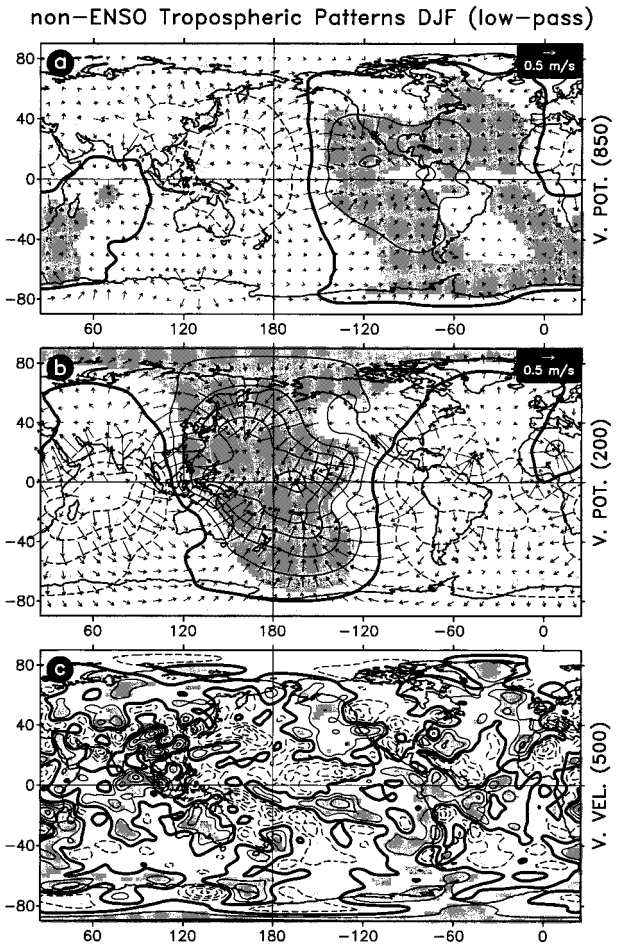

FIG. 10. Same as Fig. 9 but for the non-ENSO (low pass) residuals.

(ENSO mode removed) a similar pattern to that of ENSO is found at 850 hPa (Fig. 10a). However, the 850-hPa convergence center over the eastern equatorial Pacific (ENSO) is now split into two off-equatorial covergence regions with a stronger northern branch near the west coast of North America. This pattern is consistent with the structure of the low-pass SST composites in Fig. 7, which shows off-equatorial (decadal) warming over the eastern Pacific. The 200-hPa pattern (Fig. 10b) is very different from ENSO, being strongly skewed with respect to 850 hPa over much of the tropical strip. Where the ENSO pattern has strong divergence near 170°W, the residual shows strong convergence. Similarly, the 200-hPa flow is strongly divergent over northern South America, where anomalous convergence prevails during ENSO. Unlike ENSO, the western Indian Ocean has convergence at 850 hPa and strong divergence at 200 hPa.

The 500-hPa vertical velocity (Fig. 10c) shows little of the upward motion east of the date line seen with ENSO, but now shows much stronger uplift than normal over the Amazonian region, also opposite to ENSO. The uplift is stronger than the subsidence associated with ENSO warmings and it covers a larger area of northern South America, at least to 20°S and including northeast Brazil. Over the Indian Ocean we see uplift, which together with the horizontal flows is consistent with strengthened convection over the ocean and a stronger winter monsoon circulation. Over Australia, we also find positive vertical velocity anomalies that are opposite to ENSO, as was the case over the Amazonian region.

In contrast with the ENSO composite, the decadally dominated residual pattern shows weakened Hadley flow over the central Pacific and a strengthened meridional circulation over the tropical North Atlantic. While the 850-hPa Walker flow is weakened over the central Pacific, as in ENSO, the 200-hPa flow is now strongly weakened, causing the overall zonal anomaly to be stronger. Taken in total, the Walker and Hadley circulations are quite different in terms of the zonal flows and the polarities of the divergence centers.

If we take the transitivity of the direct circulation anomaly with respect to Niño-3 to be the ratio of the zonal variation of 200-hPa velocity potential to the rms variation of the corresponding temporal component of Niño-3, then the circulation is more than three times as responsive to the residual variability than to the ENSO component. This does not imply that the ''pound-for-pound'' climate impact of decadal variability is greater than for ENSO. It more likely reflects the fact that the equatorial projection of decadal variability is of smaller amplitude than that of the off-equatorial regions, while the reverse is true for ENSO.

We do not show the composites for the high-pass component of the residual Niño-3 variability because they are essentially featureless. This is consistent with the noiselike character of the surface composites (Fig. 6).

6. Summary and discussion

We have computed and compared the surface and tropospheric patterns associated with canonical ENSO and non-ENSO (residual) SSTA variability in the Niño-3 region (5°S–5°N, 150°–90°W) of the eastern tropical Pacific. The canonical ENSO variability was defined as the leading global complex EOF mode in the interannual (0–8 yr) band and describes well known aspects of ENSO. The non-ENSO residuals include noncanonical ENSO behavior in the interannual (0–8 yr) band as well as decadal variability with timescales longer than 8 years. In this section, we summarize and discuss our main results and compare them with the results of a similar analysis using SST averaged over the Niño-4 region (5°S–5°N, 160°E–150°W) of the central equatorial Pacific (not shown).

On decadal scales, the ENSO and the residual variability show similar patterns for SST, SLP, and surface wind stress, consistent with Zhang et al. (1997) and Garreaud and Battisti (1999). On interannual timescales, there is some indication that the residual SSTA variabilities in the eastern tropical Pacific and in the sub-

tropical western boundary current regions (i.e., Kuroshio extension and East Australia Current) may be correlated. However, the marginal significance of the midlatitude warm anomalies indicate that they may simply be attributable to geophysical noise. Consistent with this interpretation, we found no significant midlatitude warm anomalies in those regions when the analysis was repeated using SSTA averaged over the Niño-4 region.

The low-frequency behavior of the Niño-3 residual is most clearly identified with the Pacific decadal variability in SSTA described by many authors. The high-frequency portion of the variability is found to have nonstationarities, the most notable involving a significant increase in the interannual variance of the 1980s and 1990s. This increase is consistent with the obviously larger, noncanonical peaks in the Niño-3 residual during the 1982–83 and 1997–98 El Niño events (Fig. 3b). While the spatial composites based on the high-pass component (Fig. 6) are most consistent with geophysical noise, they have the effect of disguising the Pacific decadal signature that is so evident in the low-pass composites (Fig. 7).

One of the more surprising results of this analysis is that the tropospheric direct circulation responds quite differently, and more strongly, to the decadal Pacific variability (smoothed residual) than to the canonical ENSO heating. The differences are most evident in the Hadley and Walker flows at 200 hPa and in the degree of convection over the Indian Ocean, the date line, and northern South America. These distinctions cannot, of course, have anything to do with SST over the Niño-3 region itself. Indeed, similar results are found when the analysis is repeated with SST averaged over the Niño-4 region of the central Pacific. They must be due to differences in the overall distributions of SST associated with the ENSO and decadal components of Niño-3 (Figs. 4a and 7a), and/or to differences between the respective ocean–atmosphere mechanisms involved in ENSO versus the Pacific Decadal Oscillation (PDO).

At low latitudes, the implication of the contrary tropospheric behaviors is that the intensity and predictability of ENSO-related climate impacts there will vary with the phase of Pacific decadal variability. A strong El Niño, such as 1972–73, which occurs during a period of negative background SST anomalies in the eastern equatorial Pacific, can have a stronger climate response in some regions than an event that occurs in a period with warm background temperatures (such as 1982–83 or 1997–98), even though the latter events may be more intense in terms of equatorial SSTs. By the same token, the La Niña (cold) events that occur during a decadal warming phase may have stronger impacts in the same regions than during periods of cool background temperatures. The sense of climate impacts is likely to be more equivocal and less predictable when the phases of the ENSO and decadal oscillations agree (warm/warm or cold/cold) because the respective direct circulation anomalies are generally opposite.

We hasten to point out that the differences seen in this study between the divergent anomaly circulation of the canonical ENSO and the decadal variability (Figs. 9 and 10) do not necessarily extend to extratropical latitudes. Divergence-related indices at the top and bottom of the troposphere are reasonably good indicators of the typically deep convection found in the Tropics but may not reflect well the extratropical convective processes. Thus, for example, Mantua et al. (1997) and Gershunov and Barnett (1998) both observe similarities between ENSO and the PDO in the climate effects over North America. In that respect, Gershunov and Barnett reach the opposite conclusion to ours, namely that the climate patterns over North America are reinforced (more predictable) when the interannual and decadal SSTA are in the same phase over the low-latitude east Pacific. McCabe and Dettinger (1999) reach a similar conclusion about rainfall over the western half of the United States. This contrast may reflect a distinction between the Tropics and the extratropics and our results may only apply to those low-latitude regions that are strongly affected by the tropospheric direct circulation. Having made this distinction, however, we do note some similarity in the 500-hPa vertical velocity composites for ENSO and the Niño-3 residual in the North American sector (Figs. 9c and 10c). Thus, the NCEP–NCAR midtroposphere vertical velocity data are not inconsistent with the interpretation of ENSO teleconnections in the North American sector given by McCabe and Dettinger (1999) and Gershunov and Barnett (1998).

Several low-latitude regions are clearly affected by the dichotomy between the interannual and decadal components of the direct circulation. The Indian Ocean sees strengthened convection and a stronger winter monsoon over India and east Africa. The Hadley cell in the North Pacific is weakened and the one in the North Atlantic is strengthened, both opposite to the ENSO response. In terms of societal impacts (where people live), however, the distinctions are most significant in South America (north of 20°S) and over the entire Australian continent. In South America, this may account for historical inconsistencies in rainfall that have occurred over that region with respect to classical ENSO indices such as the SOI and Niño-3. This will be especially true over the north-central Amazonian region, Venezuela, and Colombia, where the anomalous vertical velocity (500 hPa) is opposite for ENSO and decadal warmings. Over northeast Brazil (where the tropospheric response to ENSO appears weak), the decadal phase in vertical velocity will also tend to have an opposite effect on rainfall to that induced by ENSO-related northward migrations of the ITCZ. In Australia, our low-latitude results are consistent with Power et al. (1999), who recently investigated the effects of the PDO on ENSO predictability of climate (rainfall, surface temperature, river flow, and domestic wheat crop yield). They concluded that when the PDO lowers (raises) temperatures in the tropical Pacific Ocean there is (is not)

a close association between year-to-year Australian climate variations and ENSO.

The tropospheric results contain a strong message for coupled ocean–atmosphere modelers and for empirically based climate predictions. If the decadal component of variability can be successfully simulated in models, the tropospheric simulation should verify significantly better than for a model that simulates ENSO alone. For some regions (e.g., northern South America and Australia), statistical prediction of rainfall based on climate indices such as the Niño-3 and SOI will be more accurate if the ENSO and decadal components of variability are accounted for separately.

Acknowledgments. We thank J. Harris for help with the NCEP–NCAR reanalysis fields. C. Wang and two anonymous reviewers provided helpful comments. We acknowledge the support of the National Oceanic and Atmospheric Administration (NOAA) through its Pan-American Climate Studies program, the Inter-American Institute for Global Change Research (IAI), and NOAA Environmental Research Laboratories through their base funding of our laboratory. This research has been carried out under the auspices of the Cooperative Institute of Marine and Atmospheric Studies (CIMAS), a joint institute of the University of Miami and NOAA, Cooperative Agreement Number NA67RJ0-149.

REFERENCES

Allan, R. J., 2000: ENSO and climatic variability in the past 150 years. *El Niño and the Southern Oscillation: Multiscale Variability and Global and Regional Impacts,* H. F. Diaz and V. Markgraf, Eds., Cambridge University Press, 3–55.

——, and R. D. D'Arrigo, 1999: 'Persistent' ENSO sequences: How unusual was the 1990–1995 El Niño? *Holocene,* **9,** 101–118.

Cardone, V. J., J. G. Greenwood, and M. A. Cane, 1990: On trends in historical marine wind data. *J. Climate,* **3,** 113–127.

Cleveland, W. S., and S. J. Devlin, 1988: Locally weighted regression: An approach to regression analysis by local fitting. *J. Amer. Stat. Assoc.,* **83,** 596–610.

da Silva, A. M., C. C. Young, and S. Levitus, 1994: *Algorithms and Procedures.* Vol. 1, *Atlas of Surface Marine Data 1994,* NOAA Atlas NESDIS 6, 83 pp.

Enfield, D. B., and D. A. Mayer, 1997: Tropical Atlantic SST variability and its relation to El Niño–Southern Oscillation. *J. Geophys. Res.,* **102,** 929–945.

——, and A. M. Mestas-Nuñez, 1999: Multiscale variabilities in global sea surface temperatures and their relationships with tropospheric climate patterns. *J. Climate,* **12,** 2719–2733.

——, and ——, 2000: Interannual-to-multidecadal climate variability and its relationship to global sea surface temperatures. *Interhemispheric Climate Linkages,* V. Markgraf, Ed., Academic Press, 17–29.

Garreaud, R. D., and D. S. Battisti, 1999: Interannual (ENSO) and interdecadal (ENSO-like) variability in the Southern Hemisphere tropospheric circulation. *J. Climate,* **12,** 2113–2123.

Gershunov, A., and T. P. Barnett, 1998: Interdecadal modulation of ENSO teleconnections. *Bull. Amer. Meteor. Soc.,* **79,** 2715–2725.

Gu, D., and S. G. H. Philander, 1997: Interdecadal climate fluctuations that depend on exchanges between the Tropics and extratropics. *Science,* **275,** 721–892.

Harrison, D. E., and N. K. Larkin, 1997: Darwin sea level pressure, 1876–1996: Evidence for climate change? *Geophys. Res. Lett.,* **24,** 1779–1782.

Kalnay, E., and Coauthors, 1996: The NCEP/NCAR 40-Year Reanalysis Project. *Bull. Amer. Meteor. Soc.,* **77,** 437–471.

Kaplan, A., M. A. Cane, Y. Kushnir, A. C. Clement, M. B. Blumenthal, and B. Rajagopalan, 1998: Analysis of global sea surface temperatures 1856–1991. *J. Geophys. Res.,* **103,** 18 567–18 589.

Kleeman, R., J. P. McCreary Jr., and B. A. Klinger, 1999: A mechanism for generating ENSO decadal variability. *Geophys. Res. Lett.,* **26,** 1743–1746.

Landsea, C. W., R. A. Pielke Jr., A. M. Mestas-Nuñez, and J. A. Knaff, 1999: Atlantic basin hurricanes: Indices of climatic changes. *Climatic Change,* **42,** 89–129.

Latif, M., and T. P. Barnett, 1994: Causes of decadal climate variability over the North Pacific and North America. *Science,* **266,** 634–637.

——, and ——, 1996: Decadal climate variability over the North Pacific and North America: Dynamics and predictability. *J. Climate,* **9,** 2407–2423.

——, R. Kleeman, and C. Eckert, 1997: Greenhouse warming, decadal variability, or El Niño? An attempt to understand the anomalous 1990s. *J. Climate,* **10,** 2221–2239.

Lau, K.-M., and H. Weng, 1999: Interanual, decadal–interdecadal, and global warning signals in sea surface temperature during 1955–97. *J. Climate,* **12,** 1257–1267.

Madden, R. A., and P. R. Julian, 1994: Observations of the 40–50-day tropical oscillation—a review. *Mon. Weather Rev.,* **122,** 814–837.

Mantua, N. J., S. R. Hare, Y. Zhang, J. M. Wallace, and R. C. Francis, 1997: A Pacific interdecadal climate oscillation with impacts on salmon production. *Bull. Amer. Meteor. Soc.,* **78,** 1069–1079.

McCabe, G. J., and M. D. Dettinger, 1999: Decadal variations in the strength of ENSO teleconnections with precipitation in the western United States. *Int. J. Climatol.,* **19,** 1399–1410.

Mestas-Nuñez, A. M., and D. B. Enfield, 1999: Rotated global modes of non-ENSO sea surface temperature variability. *J. Climate,* **12,** 2735–2746.

Parker, D. E., P. D. Jones, C. K. Folland, and A. Bevan, 1994: Interdecadal changes of surface temperature since the late nineteenth century. *J. Geophys. Res.,* **99,** 14 373–14 399.

Power, S., T. Casey, C. Folland, A. Colman, and V. Metha, 1999: Inter-decadal modulation of the impact of ENSO on Australia. *Climate Dyn.,* **15,** 319–324.

Rajagopalan, B., U. Lall, and M. A. Cane, 1997: Anomalous ENSO occurrences: An alternate view. *J. Climate,* **10,** 2351–2357.

Reynolds, R. W., and T. M. Smith, 1994: Improved global sea surface temperature analyses using optimum interpolation. *J. Climate,* **7,** 929–948.

Smith, T. M., R. E. Livezey, and S. S. Shen, 1998: An improved method for analysing sparse and irregularly distributed SST data on a regular grid: The tropical Pacific Ocean. *J. Climate,* **11,** 1717–1729.

Torrence, C., and G. P. Compo, 1998: A practical guide to wavelet analysis. *Bull. Amer. Meteor. Soc.,* **79,** 61–78.

Trenberth, K. E., and T. J. Hoar, 1996: The 1990–1995 El Niño–Southern Oscillation event: Longest on record. *Geophys. Res. Lett.,* **23,** 57–60.

——, and ——, 1997: El Niño and climate change. *Geophys. Res. Lett.,* **24,** 3057–3060.

Wang, C., R. H. Weisberg, and J. L. Virmani, 1999: Western Pacific interannual variability associated with El Niño–Southern Oscillation, *J. Geophys. Res.,* **104,** 5131–5149.

Zhang, Y., J. M. Wallace, and D. S. Battisti, 1997: ENSO-like interdecadal variability: 1990–93. *J. Climate,* **10,** 1000–1020.